INORGANIC
CHEMISTRY
FRONTIERS

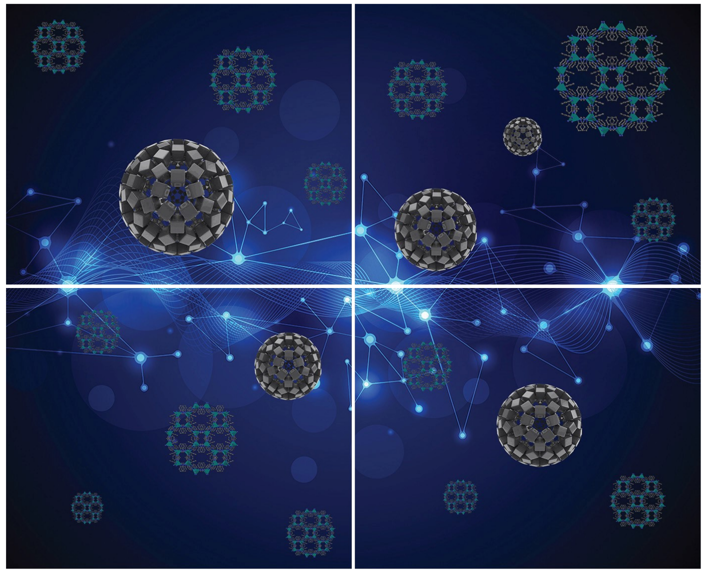

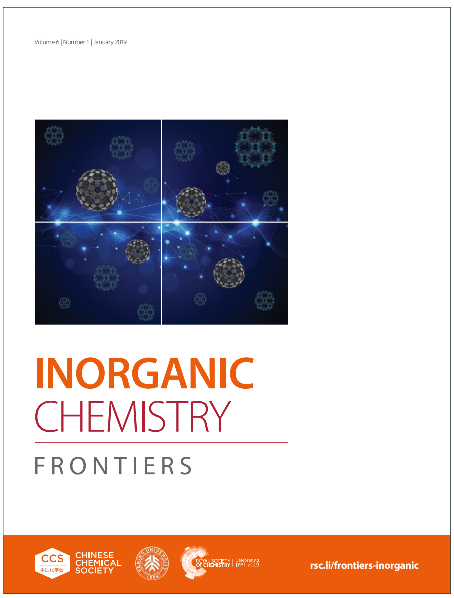

View Article Online
DOI: 10.1039/D6QI00499G

Water Splitting with Cobalt-incorporated Ruthenium Sulfide (Co_xRuS) and a Molecular Cobalt Porphyrin

Received 00th January 20xx,
Accepted 00th January 20xx

DOI: 10.1039/x0xx00000x

Nasim Jafari, Neidy Ocuane, Brenda Torres, Jose L. Lasso, Carlos R. Cabrera, Dino Villagrán*

Here we present a one-step synthesis of bimetallic cobalt ruthenium sulfide on Vulcan XC-72R carbon (C-Co_xRuS) for electrochemical water splitting, which was coupled with CoTcPP (cobalt 5,10,15,20-tetrakis(4-carboxyphenyl) porphyrin) for improved Oxygen Evolution Reaction (OER) electrocatalysis. Electrochemical analyses reveal that increasing cobalt content enhances the maximum current density by 8x for HER and 3x for OER. The optimized C-Co_4RuS catalyst demonstrates bifunctional activity with an HER overpotential of -75 mV (vs. RHE) at 10 mA cm^{-2} and a Tafel slope of 75 mV dec^{-1} for HER (Volmer-Heyrovsky mechanism) and an overpotential of 257 mV (vs. RHE) at 10 mA cm^{-2}, with a Tafel slope of 95 mV dec^{-1} for OER. The addition of cobalt to the ruthenium sulfide material facilitates charge transfer and improves active site accessibility according to Electrochemical Impedance Spectroscopy (EIS) and Electrochemical Active Surface Area (ECSA) data. Upon CoTcPP compositing the OER overpotential and Tafel plot decrease to 202 mV (vs. RHE) and 79 mV dec^{-1} further improving its catalytic activity. These findings position C-Co_xRuS/CoTcPP as an efficient, bifunctional electrocatalyst, providing a viable alternative to common electrocatalysts for water splitting in sustainable energy applications.

Introduction

Hydrogen, with a high energy density (146 kJ g^{-1}) and zero carbon emissions, has emerged as a sustainable solution to the growing problems of energy depletion and environmental contamination.[1,2] Currently, the primary method for producing hydrogen on a large scale is through the steam reforming of methane.[3] This process requires high temperature and releases significant amounts of carbon dioxide.[4] Therefore, developing efficient and environmentally sustainable hydrogen production methods is crucial.[5] Among various alternatives, water splitting into hydrogen and oxygen through electrolysis presents a promising approach to avoid these issues.[6]

Water splitting consists of two half-reactions: the hydrogen evolution reaction (HER) and the oxygen evolution reaction (OER). While HER directly produces hydrogen, OER plays a crucial role in completing the overall redox cycle.[7,8] HER and OER occur at 0 V and 1.23 V versus the reversible hydrogen electrode (RHE) at 298 K, respectively.[9] However, additional energy is often required to overcome the activation energy to initiate the reaction.[10] A key limitation in this process is the sluggish kinetics of the OER, the four-electron half reaction that significantly limits overall water splitting efficiency.[11–13] To address this bottleneck, the development of efficient electrocatalysts is critical. Electrocatalysts reduce the overpotential, enhance reaction kinetics, and improve energy conversion efficiency.[7] In designing such catalysts, factors like activity, stability, cost, and ease of synthesis must be considered.[14] Platinum-based materials are widely regarded as benchmark HER catalysts due to their performance.[15–18] However, the high cost and scarcity of platinum hinder its widespread application.[19]

Transition metal chalcogenides (TMCs), particularly sulfides, have gained interest for electrocatalysis due to their good electrical conductivity and variable oxidation states, which in turn, enhance redox activity.[20–23] Like the hydrogenase enzyme structure, the high activity of transition metal sulfides for hydrogen production is likely due to the presence of metal sulfur clusters with five ligands that are arranged in a distorted octahedral configuration.[24–26] Ruthenium disulfide (RuS_2) is a transition metal sulfide that is known for its catalytic activity in hydrodesulfurization (HDS).[27] Numerous studies have shown that catalysts effective for HDS also excel as HER electrocatalysts, as both reactions involve reversible hydrogen binding to the catalyst.[24,28] While ruthenium is classified as a precious metal, it is significantly more affordable than platinum, so ruthenium-based materials have gained attention as lower-cost alternatives for platinum in HER.[29] Recent studies have demonstrated that Ru-based nanostructures, heterostructures, and hybrid catalysts can deliver excellent hydrogen-evolution activity through optimized hydrogen adsorption energetics, improved conductivity, and reduced noble-metal loading. Representative examples include Ru-containing composite catalysts, defect-engineered Ru systems, and interfacial Ru-based electrocatalysts reported in recent literature.[30–32] Although RuS_2 has shown promise for HER-related electrocatalysis, its broader application in water splitting, particularly under anodic OER conditions, remains comparatively underexplored. Additionally, high ruthenium loadings are often required, which raises cost concerns and compromises stability under OER conditions due to the susceptibility of ruthenium to oxidation at high potentials.[33]

To improve both the activity and stability of ruthenium-based catalysts, recent efforts have focused on compositional

[a] Department of Chemistry and Biochemistry, The University of Texas at El Paso, El Paso, Texas, 79968, USA.
* Corresponding author - E-mail: dino@utep.edu
Supplementary Information available: [details of any supplementary information available should be included here]. See DOI: 10.1039/x0xx00000x

View Article Online
DOI: 10.1039/D6QI00490G

tuning.[34] Introducing a second transition metal, such as cobalt, into sulfide systems has been shown to enhance electrochemical performance through electronic modulation, broader accessible oxidation states, and narrowed band gaps compared with single-metal sulfides.[35,36] For example, cobalt ruthenium sulfide electrodes have shown promising electrochemical activities as supercapacitors, which suggests its potential for electrocatalysis.[37]

Another promising approach is incorporating porphyrin-based molecular structures[38,39]. Porphyrins are a group of highly conjugated macrocyclic compounds known for their structural versatility, chemical tunability, and stable π-conjugated systems.[40] The electronic and chemical properties of porphyrins can be precisely adjusted through metalation, peripheral functionalization, and substitution at the meso or β- positions, which in turn allow for control over redox behavior and molecular interactions.[41] As a result, porphyrins have gained attention in energy conversion applications, particularly in electrocatalysis and photoelectrocatalysis[42]. In water splitting, metalloporphyrins, such as cobalt, nickel, and iron porphyrins, have shown notable activity in OER, due to their ability to support multi-electron transfer and stabilize reactive intermediates.[43–45] Recent work has further shown that porphyrin-based metal architectures, particularly cobalt-centered systems, can promote oxygen electrocatalysis by providing structurally defined active sites and facilitating multielectron O–O bond-forming pathways, showing the broader value of tunable porphyrin motifs in water-splitting catalyst design. [46–48] Coupling these modified molecular frameworks with ruthenium sulfide can provide tunable structures and efficient electron transfer pathways that can stabilize active sites[38], while reducing the required ruthenium content.

Herein, we report a modified one-step synthesis method for cobalt ruthenium sulfide supported on carbon (C-Co$_x$RuS) as a HER/OER catalyst and its composite with cobalt porphyrin (CoTcPP) as a catalyst for OER in electrochemical water splitting (Scheme 1). The introduction of cobalt into the ruthenium sulfide matrix enhanced catalytic performance while reducing the overall ruthenium content. Furthermore, with the addition

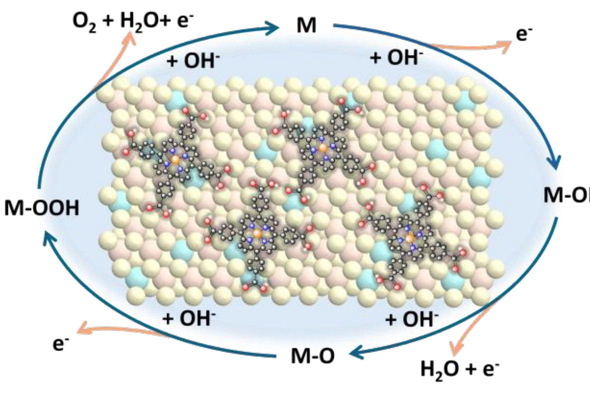

Scheme 1. Schematic illustration of Oxygen Evolution Reaction (OER) on CoTcPP/C-Co$_4$RuS catalytic surface (M represents metal active sites of Co and Ru).

of CoTcPP, the resulting composite exhibits a significantly lower OER overpotential and faster kinetics, evidenced by a smaller Tafel slope, than its constituent components. These improvements may arise from electronic interactions between the mixed-valence cobalt and ruthenium centers, which facilitate more efficient redox reactions, and the cobalt porphyrin, whose conjugated molecular structure promotes electron delocalization and enhances charge transfer. Together, these features increase the accessibility and utilization of active sites, resulting in improved electrocatalytic performance.

Experimental

Materials. Ruthenium chloride hydrate ($RuCl_3.xH_2O$), cobalt nitrate hexahydrate ($Co(NO_3)_2.6H_2O$), 4-carboxybenzaldehyde, propionic acid, and pyrrole were purchased from Sigma-Aldrich. Vulcan XC-72R carbon black powder was ordered from CABOT. Nafion was purchased from Alfa Aesar. All the chemicals were used as received without further purification.

Synthesis of C-CoRu$_x$S. C-Co$_x$RuS (x = Co/Ru molar ratio = 0, 1, 2, and 4) samples were synthesized through a modified one-step method. For C-CoRuS, C-Co$_2$RuS, and C-Co$_4$RuS, 178 mg, 118 mg, and 71 mg $RuCl_3.xH_2O$ and 250 mg, 333 mg, and 400 mg $Co(NO_3)_2.6H_2O$ were used, respectively. For C-RuS, 270 mg $RuCl_3.xH_2O$ was used. 0.5 ml DI water was added to each mixture and mixed with 200 mg Vulcan carbon. The resulting thick paste was placed in a Porcelain combustion boat and placed inside a tubular furnace. At a temperature of 300°C, a gaseous flow of 15% H_2S/H_2 was passed through the furnace with a flow rate of 400 ml/min for 3 hours. Then the furnace was cooled down, and the resulting black powders were collected for characterization.

Synthesis of cobalt 5,10,15,20-tetrakis(4-carboxyphenyl) porphyrin (CoTcPP). CoTcPP was synthesized according to the previously reported procedure.[38] 5 g of 4-carboxybenzaldehyde (33.3 mmol) was dissolved in 500 mL of propionic acid and heated to 140°C until complete dissolution. Then 2.23 g pyrrole (33.3 mmol) was added dropwise to the mixture, which was then refluxed under constant stirring for 2 hours. Then, 100 mL MeOH was added to the reaction, and the mixture was cooled down using an ice bath. The product was filtered using a medium-coarse filter frit. The solid product (H_2TcPP) was then washed with deionized water and dried under vacuum to obtain a dark purple powder. Afterward, 0.1 g H_2TcPP (0.126 mmol) and 0.0266 g anhydrous $Co(OAc)_2$ (0.15 mmol) were dissolved in 20 mL of DMF and were refluxed for one hour. After allowing the reaction mixture to cool, the resulting product was filtered, and the filtrate was washed with DI water and dried under vacuum at 80 °C. The resulting purple powder (0.089 g) with a yield of 83% was characterized by the UV-Vis technique. The UV-Vis spectrum of CoTcPP in DMF displays a pronounced Soret band around 430 nm and distinct Q bands of 550 nm and 595 nm (Figure S1), confirming the successful synthesis of CoTcPP.

Also, the CoTcPP/C-Co$_4$RuS used in this study was made through a physical mixture of 10 wt% CoTcPP with the C-Co$_4$RuS catalyst. The purpose of this combination was to investigate the functional

View Article Online
DOI: 10.1039/D6QI00499C

synergy between the molecular Co-porphyrin species (which facilitate O–O bond formation via Co–N_4 centers) and the conductive Ru–S framework (which enhances charge transport and stability).

Characterization methods. The phase identification through powder X-ray diffraction (pXRD) was conducted by a Panalytical Empyrean 2 X-ray diffractometer system, using Cu-Kα radiation (λ = 1.5416 Å) in 2θ range of 5-90 and 10-minute scans. The morphology analysis and microscopic surface image of the samples were collected using a Hitachi S4800 scanning electron microscope (SEM) coupled with a Bruker EDX XFlash 6160 energy-dispersive spectroscopy (EDS) system for elemental mapping. For this, the powdered sample was stuck on an aluminum stub using conductive carbon tape. Furthermore, transmission electron microscopy (TEM) imaging was conducted by a JEM-3200FS field emission electron microscope equipped with a field emission electron gun operating at an accelerating voltage of 300 kV, while the samples were drop-cast onto copper grids. X-ray photoelectron spectroscopy spectra (XPS) were collected on a XPS Nexsa G2 instrument for analysing the chemical composition and oxidation states of the samples. The XPS analysis was done with an Al Kα monochromatic source, with a pass energy of 50.0 eV. The binding energies were referenced to C1s at 285.0 eV.

Electrochemical measurements. Electrochemical measurements were carried out with a CH Instrument potentiostat (760E) at room temperature in a three-electrode cell. A graphite rod was used as the counter electrode for both HER and OER experiments. For HER, the electrolyte was 0.5 M H_2SO_4 aqueous solution, and the reference electrode was saturated calomel electrode (SCE), while for OER experiments the electrolyte was 1.0 M KOH aqueous solution, and a Hg/HgO (1.0 M NaOH) alkaline reference electrode. The working electrode was carbon paper coated with a drop-casted catalyst ink. The ink was made by a homogenous mixture of 5 mg of the electrocatalyst, 2.5 mg of carbon black, 5.0 µl of Nafion as a binding agent, and 1.0 ml of isopropyl alcohol. The solution was sonicated for 15 minutes to make a homogeneous solution and was pipetted on the carbon paper with a loading of 20 µl in a 1.0 x 1.0 cm^2 area. The ink was allowed to dry at room temperature for one hour to leave a uniform layer of material with a catalyst loading of 0.1 mg cm^{-2}.

Linear Sweep Voltammetry (LSV) was done at a scan rate of 5 mV s^{-1} after correcting with iR compensation, and the potential was reported versus the reversible hydrogen electrode (RHE) through the following equations:

$$E_{RHE} = E_{SCE} + 0.2415 + 0.0591 \times pH \quad (1)$$

$$E_{RHE} = E_{Alkaline} + 0.098 + 0.0591 \times pH \quad (2)$$

with a pH of 0 for HER experiments and 14 for OER.

The performance of these materials was analyzed through Tafel plots by using the stepped potentiostatic method, in which the potential change was conducted stepwise with a 30 s holding time at each potential to avoid capacitive current interruption. Then the equation η = b log j + a was applied, which describes the relationship between overpotential (η) and current density (j), where b represents the Tafel slope and a is a constant.[49] The slope of the linear region of the resulting plot is recorded as the Tafel.

Electrochemical Impedance Spectroscopy (EIS) measurements were done with a frequency range of 0.1 Hz to 100 kHz at a potential of 0.2 V at room temperature in a 4 mM solution of $Fe(CN)^{3-/4-}$ in 0.1 M KCl.

The electrochemical active surface area (ECSA) was estimated using cyclic voltammetry (CV) in a non-faradaic region at varying scan rates to determine the electrochemical double-layer capacitance (C_{dl}). From these CVs, the capacitive current at each scan rate is plotted, and the slope of the linear fit yields C_{dl}. Then, ECSA is calculated by dividing by the specific capacitance (C_s) for the catalyst material.[50]

All voltammograms in this work are presented following the U.S. (polarographic) convention, where cathodic (reductive) currents are plotted as positive and anodic (oxidative) currents as negative. The potential axis is displayed with more negative potentials toward the right and more positive potentials toward the left. This convention was used consistently throughout all figures for clarity and uniformity.[51]

Results and discussion

Characterization

Cobalt and ruthenium sulfide have been synthesized through various methods, including hydrothermal, solvothermal, colloidal, and gas-phase sulfidation techniques.[37,52–54] Among these, gas-phase sulfidation, where metal precursors are supported on a conductive substrate and converted under H_2S/H_2 flow, offers good control over phase formation and dispersion.[55] In this study, we employed a modified version of this method using a solvent-limited paste composed of cobalt and ruthenium salts with Vulcan carbon. This approach minimized solvent use, enhanced precursor dispersion, and improved contact with the support, leading to more uniform

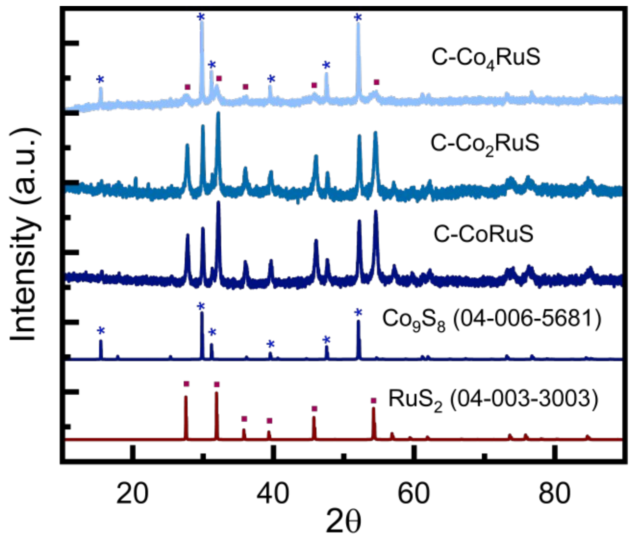

Figure 1. Powder X-ray diffraction (PXRD) of C-Co_xRuS samples, compared with the standard patterns of RuS_2 (JCPDS No. 04-003-3003, red squares) and Co_9S_8 (JCPDS No. 04-006-5681, blue asterisks), confirms that the characteristic diffraction peaks of both RuS_2 and Co_9S_8 phases are present in all samples.

View Article Online
DOI: 10.1039/D6QI00499G

sulfidation and improved electrochemical performance. The effectiveness of this synthesis method is reflected in the structural characterization of the resulting materials. Figure 1 presents the powder X-ray diffraction (PXRD) patterns of C-Co_4RuS, C-Co_2RuS, and C-CoRuS samples compared with the standard XRD patterns of RuS_2 (JCPDS No. 04-003-3003, indicated by red squares) and Co_9S_8 (JCPDS No. 04-006-5681, marked by blue asterisks). The diffraction peaks in Figure 1, at 2θ of 27.7°, 31.9°, 36.1°, 45.8°, and 54.3°, can be ascribed as (111), (200), (210), (220), (311) facets of cubic pyrite-RuS_2 (JCPDS No. 04-003-3003)[33] and 15.4°, 29.8°, 31.1°, 39.5°, 47.5° and 52° can be ascribed as (111), (311), (222), (331), (511), (440) facets of Co_9S_8 (JCPDS No. 04-006-5681).[56] All synthesized samples show characteristic peaks corresponding to both RuS_2 and Co_9S_8 phases, confirming the successful formation of a bimetallic sulfide structure. As the cobalt content increases from C-CoRuS to C-Co_4RuS, the intensity of the Co_9S_8 peaks becomes more pronounced, indicating a higher degree of cobalt in the composite. Also, the presence of sharp and well-defined peaks in all samples suggests a good crystallinity.

The morphology of C-Co_4RuS was investigated through Scanning Electron Microscopy (SEM) and Transmission Electron Microscopy (TEM) techniques. The SEM image in Figure 2a consists of polyhedral particles with sizes around 0.5-1 µm,

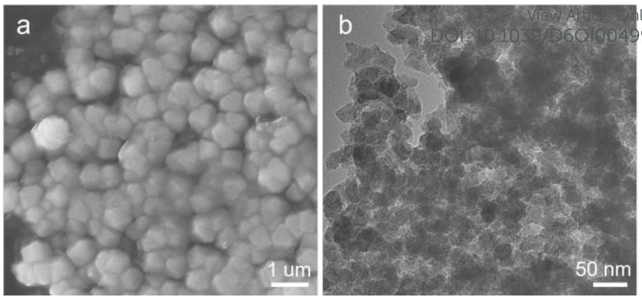

Figure 2. (a) Scanning electron microscopy (SEM) and (b) Transmission electron microscopy (TEM) images of C-Co_4RuS show polyhedral micron-sized aggregates composed of nanosized particles (5-20 nm).

while the TEM image in Figure 2b shows that these structures are composed of interconnected nanosized particles (5-20 nm). External morphology appears irregular and non-faceted due to the nature of the solid-state synthesis, which lacks morphology-directing agents. The high thermal energy promotes crystallization, while Vulcan carbon helps disperse and anchor the particles, preventing excessive sintering and supporting nanoscale structuring. This hierarchical architecture can

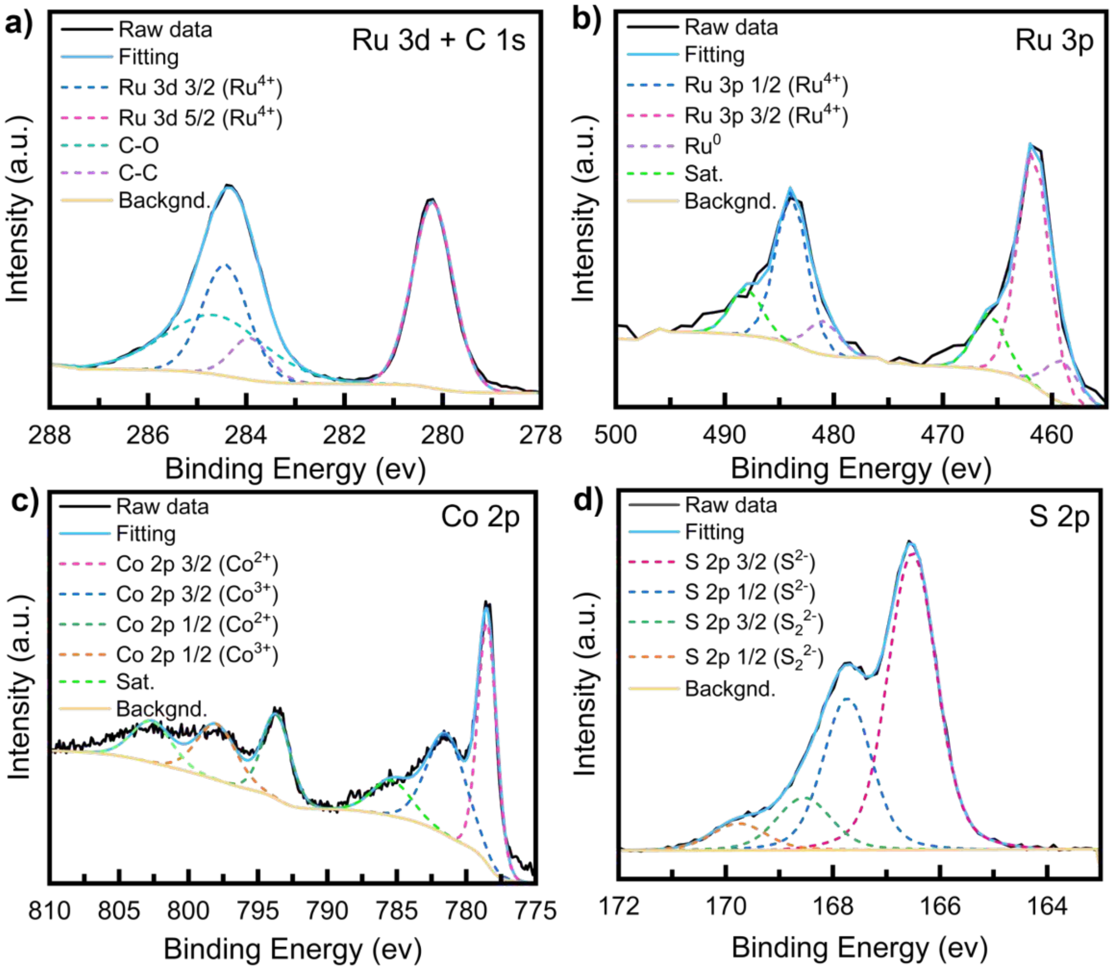

Figure 3. X-ray photoelectron spectroscopy (XPS) of C-Co_4RuS: (a) Ru 3d and C 1s, (b) Ru 3p, (c) Co 2p, and (d) S 2p binding energy regions. The Co 2p spectrum shows peaks corresponding to Co^{2+} and Co^{3+} oxidation states, while the Ru 3p and Ru 3d spectrum indicates the presence of Ru^{4+}. The S 2p region was deconvoluted into components attributed to lattice disulfide species (S_2^{2-}) and terminal sulfide species (S^{2-}). These results confirm the mixed valence states and surface composition characteristic of the bimetallic sulfide catalyst.

enhance electrochemical performance by providing high accessible active sites and improved electron transport pathways. Furthermore, the energy-dispersion X-ray spectroscopy (EDS) mapping (Figure S2) confirms that Ru, S, and Co elements are uniformly distributed over the carbon paper electrode.

The surface of the synthesized C-Co_4RuS nanoparticles was analyzed using x-ray photoelectron spectroscopy (XPS). Figure 3 (a) to (d) shows multiple deconvoluted peaks for each element. The deconvoluted Ru 3d spectrum (Figure 3a) reveals two distinct peaks at 280.2 and 284.6 eV associated with Ru $3d_{5/2}$ and Ru $3d_{3/2}$ states, respectively. Further confirmation was obtained from the Ru 3p spectrum (Figure 3b), which displays peaks at 461.8 and 484.4 eV, assigned to the Ru $3p_{3/2}$ and Ru $3p_{1/2}$ states, respectively.[57] These peaks suggest that the valence state of ruthenium in this sample is 4+.[19,58] In the Co 2p spectrum (Figure 3c), multiple features observed at 778-785 eV and 793-803 eV are attributed to Co $2p_{3/2}$ and Co $2p_{1/2}$, respectively, along with distinct satellite peaks, which are characteristic of both Co^{2+} and Co^{3+} oxidation states.[59] This indicates a mixed-valence cobalt environment within the sulfide lattice. The high-resolution S 2p spectrum (Figure 3d) was deconvoluted into two sulfur doublets corresponding to different sulfur chemical environments. The peaks at lower binding energy are assigned to terminal sulfide species (S^{2-}), while the higher-binding-energy doublet is attributed to disulfide species (S_2^{2-}) associated with the metal sulfide framework.[60] Overall, the XPS results confirm the successful incorporation of cobalt and ruthenium into the sulfide framework with mixed oxidation states, which may contribute to enhanced catalytic activity by facilitating redox activity and improved electronic conductivity.

Electrocatalytic performance

The molar ratio of Co:Ru affects the performance of final electrocatalyst, including the current density, overpotential and Tafel slope, so ideally, decreasing the amount of ruthenium while maintaining its catalytic behavior is desired. For this purpose, different ratios of $Co(NO_3)_2.6H_2O$: $RuCl_3.xH_2O$ of 4:1,

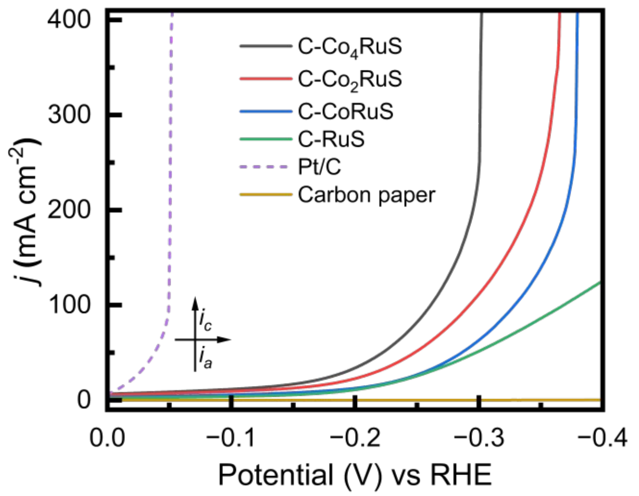

Figure 4. Linear sweep voltammetry (LSV) curves for C-Co_xRuS catalysts toward the hydrogen evolution reaction (HER) in acidic medium (H_2SO_4 0.5 M) and scan rate of 5 mV s^{-1} (as referenced by potential vs RHE).

View Article Online
DOI: 10.1039/D6QI00499G

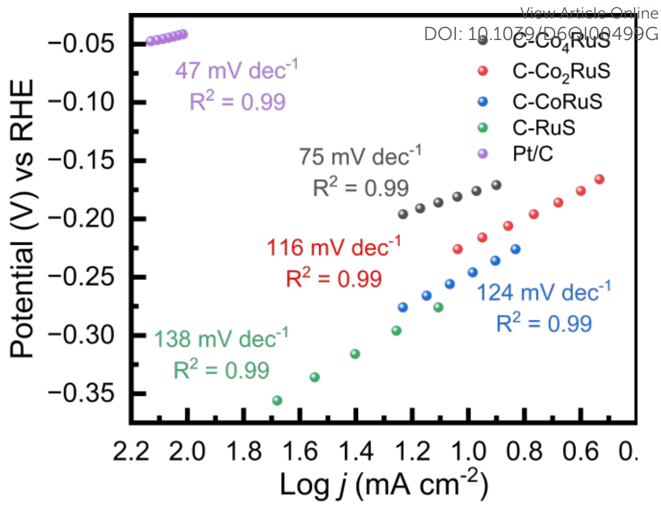

Figure 5. Tafel plots of C-Co_xRuS for hydrogen evolution reaction (HER) in H_2SO_4 0.5 M. The Tafel slopes demonstrate that C-Co_4RuS (75 mV dec^{-1}) exhibits significantly enhanced HER kinetics compared to samples with lower cobalt content and approaches the performance of the benchmark Pt/C catalyst (47 mV dec^{-1}).

2:1, 1:1 and 0:1 were composited with a similar amount of Vulcan carbon in the same flow rate of H_2S. The HER catalytic performance of C-Co_xRuS samples with different Co:Ru ratios and commercial 20% Pt/C was recorded for comparison. The resulting LSV (Linear Sweep Voltammetry) curves were normalized based on the geometrical surface area of the working electrode and were scanned with a scan rate of 5 mV s^{-1}. Figure 4 shows LSV curves for C-Co_xRuS toward the HER in acidic medium (H_2SO_4 0.5 M). Cobalt notably boosts the HER activity of ruthenium sulfide, with C-Co_4RuS performing almost as well as the commercial Pt/C catalyst. Also, the overpotential at 10 mA cm^{-2} for C-Co_4RuS (-75 mV) is significantly lower than the C-RuS (-194 mV). The Tafel plots in Figure 5 further explore the HER kinetics of the synthesized catalysts. Commercial 20% Pt/C shows a Tafel slope of 47 mV dec^{-1}, consistent with its well-known catalytic behavior. C-Co_4RuS has a Tafel slope of 75 mV dec^{-1}, indicating significantly enhanced HER kinetics compared to C-Co_2RuS (116 mV dec^{-1}), C-CoRuS (124 mV dec^{-1}), and C-RuS (138 mV dec^{-1}). This highlights the positive effect of increasing cobalt content on HER kinetics, which suggests that cobalt incorporation improves the kinetics by facilitating faster charge transfer. The Tafel slope can be utilized to characterize the mechanism of HER and its rate-limiting step. In HER, the Volmer step involves the electrochemical adsorption of hydrogen ($H^+ + e^- \rightarrow H^*$), while the Heyrovsky step refers to the electrochemical desorption of hydrogen ($H^* + H^+ + e^- \rightarrow H_2$), and in some systems, two adsorbed hydrogen atoms combine in the Tafel step ($H^* + H^* \rightarrow H_2$).[61] Based on the Tafel slopes, all synthesized samples in this work follow a Volmer-Heyrovsky mechanism, which means they facilitate HER via proton adsorption followed by electrochemical desorption, rather than H^* recombination.[62,63]

The polarization curves and Tafel plots in Figure 6 (a to c) compare the oxygen evolution reaction (OER) activity of various catalysts. In Figure 6a, C-Co_4RuS demonstrates the highest current density and the lowest overpotential among the others,

View Article Online
DOI: 10.1039/D6QI00499G

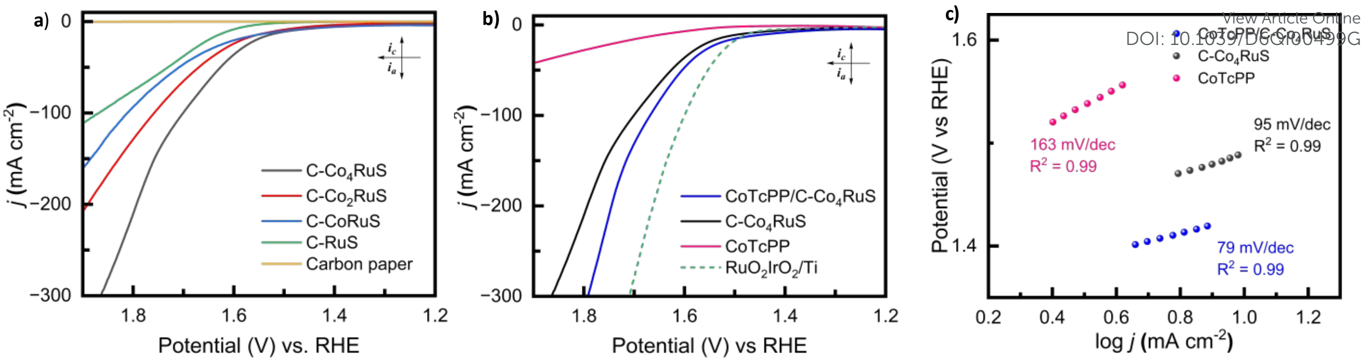

Figure 6. (a) OER polarization curves of C-Co_4RuS, C-Co_2RuS, C-CoRuS, C-RuS, and carbon paper in KOH 1.0 M, showing enhanced activity with increasing cobalt content. (b) Comparative polarization curves of C-Co_4RuS, CoTcPP, and CoTcPP/C-Co_4RuS catalyst and a commercial RuO_2–IrO_2/Ti benchmark electrode in 1.0 M KOH, demonstrating the improvement in OER performance upon CoTcPP modification. (c) Corresponding OER Tafel plots in KOH 1.0 M, where CoTcPP/C-Co_4RuS exhibits the lowest Tafel slope (79 mV dec^{-1}), confirming faster reaction kinetics compared to individual components.

indicating the positive effect of cobalt incorporation on OER performance.

As shown in Figure 6b, further modification of C-Co_4RuS was made through physical mixture with 10 wt% CoTcPP (CoTcPP/C-Co_4RuS), resulting in enhanced activity compared with pristine C-Co4RuS and CoTcPP alone, indicating that combining the porphyrin with the sulfide-derived framework provides a beneficial composite effect. The purpose of this combination was to investigate the functional synergy between the molecular Co-porphyrin species (which facilitate O–O bond formation via Co–N_4 centers) and the conductive Ru–S framework (which enhances charge transport and stability).

However, while the CoTcPP/Co_4RuS composite has enhanced OER activity, its HER activity was not improved compared to C-Co_4RuS. Yet, the composite catalyst achieves an OER overpotential of 202 mV at 10 mA cm^{-2}, which is significantly lower than that of CoTcPP (409 mV) and C-Co_4RuS (257 mV), highlighting the improved performance arising from their combination. Also, for further benchmarking, a commercial RuO_2–IrO_2/Ti electrode was evaluated under identical conditions in 1.0 M KOH, showing that the CoTcPP/C-Co_4RuS composite exhibits competitive OER activity while outperforming the parent C-Co_4RuS catalyst. The Tafel plots in Figure 6c reveal that CoTcPP/C-Co_4RuS exhibits the smallest Tafel slope (79 mV dec^{-1}), lower than C-Co_4RuS (95 mV dec^{-1}) and CoTcPP (163 mV dec^{-1}), indicating faster reaction kinetics and more efficient charge transfer in the composite catalyst. Together, these results highlight the effectiveness of cobalt and porphyrin modification in improving the OER activity of ruthenium sulfide while retaining a relatively low nominal Ru loading (Table S1). Also, as summarized in Table S3, the CoTcPP/C-Co_4RuS catalyst developed in this work delivers an OER overpotential of 202 mV at 10 mA cm^{-2} in 1.0 M KOH, which is competitive with several reported Ru-based catalysts in alkaline media. These results suggest that cobalt incorporation and CoTcPP modification improve the utilization efficiency of ruthenium while maintaining strong OER activity.

To evaluate the overall water splitting performance, the system was tested in a three-electrode configuration using CoTcPP/C-Co_4RuS as the working electrode and C-Co_4RuS as the counter electrode in KOH 1.0 M. As illustrated in Figure S3, the modified electrode system exhibited improved electrocatalytic behavior, reflected by the increased current response during the measurement. The overpotential required to reach 10 mA cm^{-2} was 190 mV, demonstrating that the use of both modified electrodes enhances the overall water-splitting activity.

To better understand the interfacial electron-transfer characteristics of the catalysts, electrochemical impedance spectroscopy (EIS) was carried out in 5 mM $[Fe(CN)_6]^{3-/4-}$ in 0.1 M KCl solution redox probe (at 0.2 V vs Ag/AgCl), to compare the behavior of the electrodes after each modification step under identical conditions. This measurement was used as a conventional indicator of the relative electron-transfer capability of the electrode surface, rather than as a direct measure of HER or OER kinetics.[64,65] The results are shown as Nyquist plots in Figure 7. In these plots, a smaller semicircle in the high-frequency region corresponds to a lower charge-transfer resistance (R_{ct}), indicating more efficient electron transfer toward the redox probe.[66] The experimental data were fitted using the equivalent circuit model (Figure S4), and the fitted parameters are summarized in Table S2. As shown in Figure 7, bare carbon paper exhibits a large

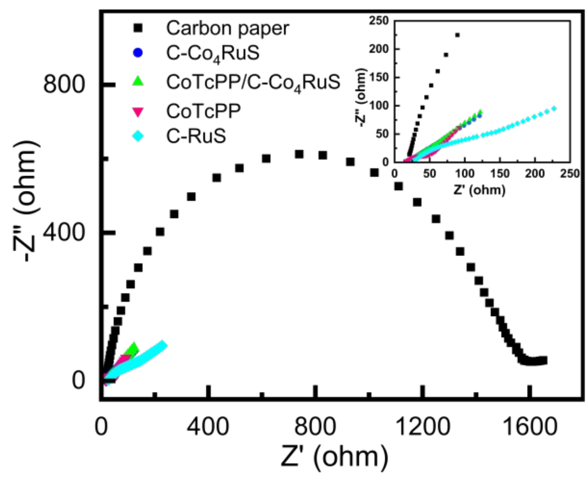

Figure 7. Nyquist plots of Carbon paper, C-RuS, C-Co_4RuS, CoTcPP, and CoTcPP/C-Co_4RuS obtained from EIS measurements in 5 mM $[Fe(CN)_6]^{3-/4-}$ in 0.1 M KCl solution redox probe (at 0.2 V vs Ag/AgCl). The smaller semicircle observed for CoTcPP/C-Co_4RuS indicates the lowest charge transfer resistance (R_{ct}) confirming faster interfacial electron transfer compared to the other samples.

semicircle and high R_{ct} (1495 Ω), reflecting relatively poor interfacial electron transfer in the probe electrolyte. Upon introduction of ruthenium and cobalt sulfide, R_{ct} decreased significantly, with C-Co_4RuS showing R_{ct} of 18.1 Ω. The incorporation of CoTcPP further enhanced the interfacial electron-transfer response, with the CoTcPP/C-Co_4RuS composite displaying the lowest R_{ct} value of 12.79 Ω. This reduction in R_{ct}, along with increased CPE values, suggests improved electronic conductivity. The improved performance of cobalt ruthenium sulfide may be attributed to the combined effect of multivalent cobalt and ruthenium species, which facilitate charge transport within the catalyst framework.

These results align with previous studies on related Ru–Co systems, which have shown that Co incorporation can modify the electronic structure of neighboring Ru sites, enriching the electron density around Ru and suppressing its over-oxidation during catalysis.[67] Additionally, the conjugated structure of CoTcPP enhances electronic delocalization, further improving charge transport and catalytic activity.

The electrochemically active surface area (ECSA) was estimated using cyclic voltammetry at scan rates of 20, 40, 60, 80, and 100 mV s^{-1} within the non-Faradaic potential region for C-C_4RuS, CoTcPP, and CoTcPP/C-Co_4RuS composite, as shown in Figures S5 to S7. In this region, where no redox reaction occurs, the measured current is directly proportional to the double-layer capacitance (C_{dl}), which serves as an indicator of the number of accessible electrochemically active sites on the catalyst surface.[68] The C_{dl} valsues were extracted from the slopes of the linear fits in plots of the current density difference ($\Delta j = (j_a - j_c)/2$) versus scan rates (Figure 8). ECSA was then calculated using the relation ECSA = C_{dl}/C_s, where C_s is the specific capacitance, typically assumed to be 40 µF cm^{-2} for a smooth surface in 1.0 M KOH. The calculated C_{dl} values were 221.6, 397.2, and 485.1 µF cm^{-2} for CoTcPP, C-Co_4RuS, and CoTcPP/C-Co_4RuS, corresponding to the ECSA values of 5.54, 9.93, and 12.13 cm^2, respectively. The CoTcPP/C-Co_4RuS composite exhibited the highest C_{dl} value, indicating the largest electrochemically accessible interfacial area among the samples studied. These results suggest that incorporation of CoTcPP increases the number of exposed catalytic sites, which contributes to enhanced OER performance. Moreover, the ECSA-normalized OER curves (Figure S8) show that the composite still exhibits higher activity after normalization, indicating that the enhancement can be attributed to interfacial interactions between CoTcPP and C-Co_4RuS.

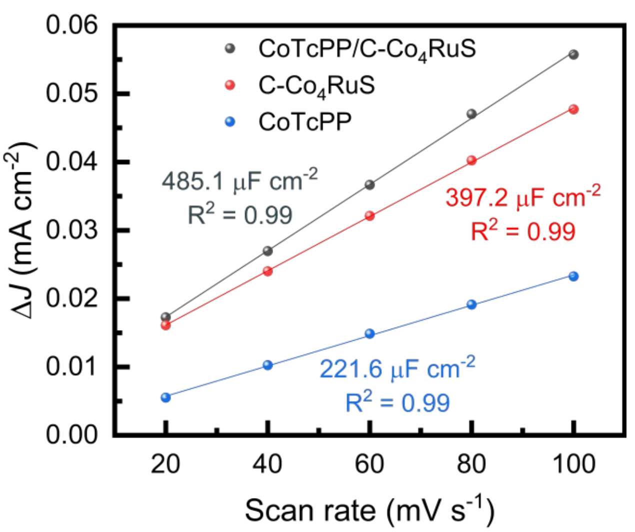

Figure 8. Plots of current density difference ($\Delta j = (j_a - j_c)/2$) versus scan rate for CoTcPP (blue), C-Co_4RuS (red), and CoTcPP/C-Co_4RuS (gray) measured in the non-Faradaic region in 1.0 M KOH. The slopes of the linear fits correspond to the double-layer capacitance (C_{dl}), indicating an increase in electrochemical active surface area (ECSA) upon porphyrin incorporation.

View Article Online
DOI: 10.1039/D6QI00489C

The ability of a catalyst to maintain its performance during electrochemical reactions is another important factor to consider. For this purpose, the electrochemical stability of the catalyst was tested for 0.1 mg cm^{-2} C-Co_4RuS and 0.1 mg cm^{-2} CoTcPP/C-Co_4RuS on carbon paper for HER and OER, respectively. The long-term potentiostatic stability tests were carried out at fixed potentials, and the current density was monitored over 20 hours. The applied potentials were chosen slightly beyond the onset potential and near the potential required to achieve 10-15 mA cm^{-2}, to ensure stable operation in the kinetic regime, minimize transient current fluctuations, and avoid mass-transport limitations (-0.14 V vs RHE for HER and 1.52 V vs RHE for OER). As shown in Figures S9 and S10, the current density is stable during both HER and OER for these time durations. The OER current density of the CoTcPP/C-Co_4RuS composite decreases by only 3% in 25 hours, which can be attributed to the protective and conductive role of the CoTcPP moiety. While the stability of ruthenium sulfide under oxidative conditions is typically limited,[69] in this work, combining it with CoTcPP significantly improved its durability. The porphyrin likely mitigates surface passivation, preserving the catalytic performance during prolonged OER operation.

To evaluate the surface chemical stability of the catalyst after long-term operation, XPS spectra were collected before and after 25 h of bulk electrolysis in oxidative conditions. As shown in Figure S11, the characteristic signals of the catalyst are still observed after the durability test, indicating that the main chemical framework is largely preserved. However, minor changes in peak shape and broadening can be seen after electrolysis, suggesting modification of the surface chemical environment during operation. The detected oxygen peak in the electrocatalyst is likely due to the presence of unavoidable oxide species or surface oxidation occurring during exposure to air.[61] Overall, the post-test XPS results indicate that the catalyst maintains its overall composition after 25 h of electrolysis, while undergoing surface evolution that may be associated with the formation of the real active species during catalysis.

Finally, another parameter that can confirm stability is Faradaic efficiency (FE). This parameter shows how much of the produced current accounts for hydrogen or oxygen production. A high Faradaic efficiency reflects minimal side reactions and excellent selectivity toward the targeted electrochemical process. Faradaic efficiency measurements for HER and OER were conducted in a sealed two-compartment H-cell separated by a Nafion membrane using 1.0 M KOH electrolyte for OER and 0.5 M H_2SO_4 electrolyte for HER. Constant-potential electrolysis was performed at 1.52 V vs. RHE in KOH 1.0 M for OER and -0.14 V vs RHE in 0.5 M H_2SO_4 for HER for 10 h. The evolved gases were sampled from the headspace using a gas-tight syringe and analyzed by gas chromatography (Shimadzu GC-8A, TCD detector). The Faradaic efficiency was calculated according to:

$$FE_{H_2}(\%) = \frac{2Fn_{H_2}}{Q} \times 100 \quad (3)$$

$$FE_{O_2}(\%) = \frac{4Fn_{O_2}}{Q} \times 100 \quad (4)$$

where F is Faraday's constant, n is measured gas moles, and Q is total charge passed. In this study, the Faradaic efficiency for HER was measured to be 96% with C-Co_4RuS, and the CoTcPP/C-Co_4RuS composite had an FE of 95%, confirming that most of the charge passed during electrolysis contributes directly to water splitting, validating the high efficiency and stability of the catalyst.

Overall, electrochemical analyses confirm that combining the multivalent nature of cobalt with ruthenium sulfide enhances both HER and OER performance, while further integration with cobalt porphyrin produces an even more active and durable electrocatalyst for OER. This synergy lowers overpotentials and accelerates reaction kinetics by improving charge-transfer efficiency and increasing active-site accessibility. Stability tests reveal minimal performance loss during prolonged operation, effectively mitigating the oxidative instability typically associated with ruthenium-based catalysts. These results position CoTcPP/C-Co_4RuS as a promising candidate for efficient and scalable water-splitting applications.

Conclusions

In summary, we have developed a one-step, solvent-limited synthetic method to prepare a bimetallic cobalt-ruthenium sulfide electrocatalyst supported on carbon (C-Co_4RuS), as well as its composite with a molecular catalyst, a cobalt-based porphyrin (CoTcPP), for efficient water splitting. The C-Co_4RuS catalyst demonstrates promising HER activity, exhibiting an overpotential of -75 mV at 10 mA cm^{-2} and a Tafel slope of 75 mV dec^{-1} in comparison to C-RuS synthesized through the same method with an overpotential of -194 mV and a Tafel slope of 138 mV dec^{-1}. In the OER experiment, C-Co_4RuS, shows an overpotential of 257 mV at 10 mA cm^{-2} with a Tafel slope of 95 mV dec^{-1}. Upon addition of 10% of CoTcPP, the CoTcPP/C-Co_4RuS composite exhibits a reduction of 19% in the overpotential (202 mV) and a 17% improvement in Tafel slope (79 mV dec^{-1}). This improved performance is attributed to the complementary combination between the multivalent metal chalcogenides and the porphyrin units, which facilitates charge transfer, increases the number of active sites, and preserves stability. These findings demonstrate the potential of integrating molecular catalysts with heterogeneous systems to develop efficient water splitting electrocatalysts.

Author contributions

Conceptualization and project administration - Nasim Jafari, Brenda Torres, Dino Villagrán. Methodology, data curation and investigation - Nasim Jafari, Neidy Ocuane, Jose L. Lasso, Brenda Torres. Validation and resources - Dino Villagrán, Brenda Torres, Carlos R. Cabrera. Funding acquisition and supervision - Dino Villagrán. Writing original draft - Nasim Jafari. Review and editing - Nasim Jafari, Neidy Ocuane, Dino Villagrán.

Conflicts of interest

There are no conflicts to declare.

Data availability

The data supporting this article have been included as part of the Supplementary Information.

Acknowledgements

This work was supported by Cleantech (FWP 100898) funded by the U.S. Department of Energy, Office of Science, Basic Energy Sciences, and the Welch Foundation (AH-2083-2024-04-04). We also acknowledge financial support from NSF for the acquisition of the XPS equipment (NSF/CHEM 2216473) and the support of the Center for Alkaline-Based Energy Solutions (CABES), an Energy Frontier Research Center funded by the U.S. Department of Energy (DOE), Office of Science, Basic Energy Sciences (BES), under Award # DE-SC0019445.

Notes and references

(1) Chu, S.; Cui, Y.; Liu, N. The Path towards Sustainable Energy. *Nature Mater* **2017**, *16* (1), 16–22. https://doi.org/10.1038/nmat4834.
(2) Bae, S.-Y.; Mahmood, J.; Jeon, I.-Y.; Baek, J.-B. Recent Advances in Ruthenium-Based Electrocatalysts for the Hydrogen Evolution Reaction. *Nanoscale Horiz.* **2020**, *5* (1), 43–56. https://doi.org/10.1039/C9NH00485H.
(3) Dawood, F.; Anda, M.; Shafiullah, G. M. Hydrogen Production for Energy: An Overview. *International Journal of Hydrogen Energy* **2020**, *45* (7), 3847–3869. https://doi.org/10.1016/j.ijhydene.2019.12.059.
(4) Dehghanimadvar, M.; Shirmohammadi, R.; Sadeghzadeh, M.; Aslani, A.; Ghasempour, R. Hydrogen Production Technologies: Attractiveness and Future Perspective. *Int J Energy Res* **2020**, *44* (11), 8233–8254. https://doi.org/10.1002/er.5508.
(5) Jeje, S. O.; Marazani, T.; Obiko, J. O.; Shongwe, M. B. Advancing the Hydrogen Production Economy: A Comprehensive Review of Technologies, Sustainability, and Future Prospects. *International Journal of Hydrogen Energy* **2024**, *78*, 642–661. https://doi.org/10.1016/j.ijhydene.2024.06.344.

(6) Wang, J.; Xu, F.; Jin, H.; Chen, Y.; Wang, Y. Non-Noble Metal-based Carbon Composites in Hydrogen Evolution Reaction: Fundamentals to Applications. *Advanced Materials* **2017**, *29* (14), 1605838. https://doi.org/10.1002/adma.201605838.

(7) Raveendran, A.; Chandran, M.; Dhanusuraman, R. A Comprehensive Review on the Electrochemical Parameters and Recent Material Development of Electrochemical Water Splitting Electrocatalysts. *RSC Adv.* **2023**, *13* (6), 3843–3876. https://doi.org/10.1039/D2RA07642J.

(8) Ying, J.; Chen, J.-B.; Xiao, Y.-X.; Cordoba De Torresi, S. I.; Ozoemena, K. I.; Yang, X.-Y. Recent Advances in Ru-Based Electrocatalysts for Oxygen Evolution Reaction. *J. Mater. Chem. A* **2023**, *11* (4), 1634–1650. https://doi.org/10.1039/D2TA07196G.

(9) Nishioka, S.; Osterloh, F. E.; Wang, X.; Mallouk, T. E.; Maeda, K. Photocatalytic Water Splitting. *Nat Rev Methods Primers* **2023**, *3* (1). https://doi.org/10.1038/s43586-023-00226-x.

(10) Li, W.; Tian, H.; Ma, L.; Wang, Y.; Liu, X.; Gao, X. Low-Temperature Water Electrolysis: Fundamentals, Progress, and New Strategies. *Mater. Adv.* **2022**, *3* (14), 5598–5644. https://doi.org/10.1039/D2MA00185C.

(11) Fei, L.; Sun, H.; Li, Y.; Gu, Y.; Zhou, W.; Shao, Z. Recent Advances in Innovative Systems for Electrocatalytic Hydrogen Production. *Energy Environ. Sci.* **2025**, *18* (13), 6456–6529. https://doi.org/10.1039/D4EE03084B.

(12) Yu, Y.; Li, G.; Xiao, Y.; Chen, C.; Bai, Y.; Wang, T.; Li, J.; Hua, Y.; Wu, D.; Rao, P.; Deng, P.; Tian, X.; Yuan, Y. Iridium-Based Electrocatalysts for Acidic Oxygen Evolution Reaction. *Journal of Energy Chemistry* **2025**, *103*, 200–224. https://doi.org/10.1016/j.jechem.2024.11.033.

(13) Wu, C.; Yu, Y.; Song, Y.; Rao, P.; Han, X.; Liang, Y.; Li, J.; Zhang, K.; Zhang, Z.; Deng, P.; Tian, X.; Wu, D. Pyrrole-Type TM-N3 Sites as High-Efficient Bifunctional Oxygen Reactions Electrocatalysts: From Theoretical Prediction to Experimental Validation. *Journal of Energy Chemistry* **2025**, *104*, 472–481. https://doi.org/10.1016/j.jechem.2025.01.002.

(14) Qadeer, M. A.; Zhang, X.; Farid, M. A.; Tanveer, M.; Yan, Y.; Du, S.; Huang, Z.-F.; Tahir, M.; Zou, J.-J. A Review on Fundamentals for Designing Hydrogen Evolution Electrocatalyst. *Journal of Power Sources* **2024**, *613*, 234856. https://doi.org/10.1016/j.jpowsour.2024.234856.

(15) Cheng, N.; Stambula, S.; Wang, D.; Banis, M. N.; Liu, J.; Riese, A.; Xiao, B.; Li, R.; Sham, T.-K.; Liu, L.-M.; Botton, G. A.; Sun, X. Platinum Single-Atom and Cluster Catalysis of the Hydrogen Evolution Reaction. *Nat Commun* **2016**, *7* (1), 13638. https://doi.org/10.1038/ncomms13638.

(16) Subbaraman, R.; Tripkovic, D.; Strmcnik, D.; Chang, K.-C.; Uchimura, M.; Paulikas, A. P.; Stamenkovic, V.; Markovic, N. M. Enhancing Hydrogen Evolution Activity in Water Splitting by Tailoring Li^+-$Ni(OH)_2$-Pt Interfaces. *Science* **2011**, *334* (6060), 1256–1260. https://doi.org/10.1126/science.1211934.

(17) Tiwari, J. N.; Sultan, S.; Myung, C. W.; Yoon, T.; Li, N.; Ha, M.; Harzandi, A. M.; Park, H. J.; Kim, D. Y.; Chandrasekaran, S. S.; Lee, W. G.; Vij, V.; Kang, H.; Shin, T. J.; Shin, H. S.; Lee, G.; Lee, Z.; Kim, K. S. Multicomponent Electrocatalyst with Ultralow Pt Loading and High Hydrogen Evolution Activity. *Nat Energy* **2018**, *3* (9), 773–782. https://doi.org/10.1038/s41560-018-0209-x.

(18) Smiljanić, M.; Panić, S.; Bele, M.; Ruiz-Zepeda, F.; Pavko, L.; Gašparič, L.; Kokalj, A.; Gaberšček, M.; Hodnik, N. Improving the HER Activity and Stability of Pt Nanoparticles by Titanium Oxynitride Support. *ACS Catal.* **2022**, *12* (20), 13021–13033. https://doi.org/10.1021/acscatal.2c03214.

(19) Li, P.; Duan, X.; Wang, S.; Zheng, L.; Li, Y.; Duan, H.; Kuang, Y.; Sun, X. Amorphous Ruthenium-Sulfide with Isolated Catalytic Sites for Pt-Like Electrocatalytic Hydrogen Production Over Whole pH Range. *Small* **2019**, *15* (46). https://doi.org/10.1002/smll.201904043.

(20) Sahoo, S.; Pazhamalai, P.; Krishnamoorthy, K.; Kim, S.-J. Hydrothermally Prepared α-MnSe Nanoparticles as a New Pseudocapacitive Electrode Material for Supercapacitor. *Electrochimica Acta* **2018**, *268*, 403–410. https://doi.org/10.1016/j.electacta.2018.02.116.

(21) Raman, V.; Chinnadurai, D.; Rajmohan, R.; Chebrolu, V. T.; Rajangam, V.; Kim, H.-J. Transition Metal Chalcogenide Based MnSe Heterostructured with $NiCo_2O_4$ as a New High Performance Electrode Material for Capacitive Energy Storage. *New J. Chem.* **2019**, *43* (32), 12630–12640. https://doi.org/10.1039/C9NJ02711D.

(22) Ge, Y.; Wu, Y.; Ma, L.; Li, X. (James); Román, M.; Chianelli, R. R.; Torres, B.; Villagrán, D. Amine and Carbon-Pretreated Nickel–Molybdenum Disulfide as Bifunctional Electrocatalysts for Hydrogen and Oxygen Gas Evolution. *International Journal of*

View Article Online
DOI: 10.1039/D6QI00499G

Hydrogen Energy **2022**, *47* (65), 27839–27847. https://doi.org/10.1016/j.ijhydene.2022.06.114.

(23) Feng, S.; Rao, P.; Wu, X.; Li, K.; Qi, A.; Yu, Y.; Li, J.; Deng, P.; Yuan, Y.; Wang, S.; Tian, X.; Kang, Z. *In-situ* Generation of Hydroxyl Layers in CoO @ $FeSe_2$ Catalyst for High Selectivity Seawater Electrolysis. *Chin. J. Chem.* **2024**, *42* (1), 48–54. https://doi.org/10.1002/cjoc.202300441.

(24) Yu, J.; Guo, Y.; Miao, S.; Ni, M.; Zhou, W.; Shao, Z. Spherical Ruthenium Disulfide-Sulfur-Doped Graphene Composite as an Efficient Hydrogen Evolution Electrocatalyst. *ACS Appl. Mater. Interfaces* **2018**, *10* (40), 34098–34107. https://doi.org/10.1021/acsami.8b08239.

(25) Shima, S.; Pilak, O.; Vogt, S.; Schick, M.; Stagni, M. S.; Meyer-Klaucke, W.; Warkentin, E.; Thauer, R. K.; Ermler, U. The Crystal Structure of [Fe]-Hydrogenase Reveals the Geometry of the Active Site. *Science* **2008**, *321* (5888), 572–575. https://doi.org/10.1126/science.1158978.

(26) Wang, D.-Y.; Gong, M.; Chou, H.-L.; Pan, C.-J.; Chen, H.-A.; Wu, Y.; Lin, M.-C.; Guan, M.; Yang, J.; Chen, C.-W.; Wang, Y.-L.; Hwang, B.-J.; Chen, C.-C.; Dai, H. Highly Active and Stable Hybrid Catalyst of Cobalt-Doped FeS_2 Nanosheets–Carbon Nanotubes for Hydrogen Evolution Reaction. *J. Am. Chem. Soc.* **2015**, *137* (4), 1587–1592. https://doi.org/10.1021/ja511572q.

(27) Kuo, Y. Hydrogenation and Hydrodesulfurization over Sulfided Ruthenium Catalysts II. Impact of Surface Phase Behavior on Activity and Selectivity. *Journal of Catalysis* **1988**, *112* (1), 250–266. https://doi.org/10.1016/0021-9517(88)90138-8.

(28) Popczun, E. J.; McKone, J. R.; Read, C. G.; Biacchi, A. J.; Wiltrout, A. M.; Lewis, N. S.; Schaak, R. E. Nanostructured Nickel Phosphide as an Electrocatalyst for the Hydrogen Evolution Reaction. *J. Am. Chem. Soc.* **2013**, *135* (25), 9267–9270. https://doi.org/10.1021/ja403440e.

(29) Yang, Y.; Yu, Y.; Li, J.; Chen, Q.; Du, Y.; Rao, P.; Li, R.; Jia, C.; Kang, Z.; Deng, P.; Shen, Y.; Tian, X. Engineering Ruthenium-Based Electrocatalysts for Effective Hydrogen Evolution Reaction. *Nano-Micro Lett.* **2021**, *13* (1), 160. https://doi.org/10.1007/s40820-021-00679-3.

(30) Smiljanić, M.; Bele, M.; Pavko, L.; Hrnjić, A.; Ruiz-Zepeda, F.; Bijelić, L.; Kamšek, A. R.; Nuhanović, M.; Marsel, A.; Gašparič, L.; Kokalj, A.; Hodnik, N. Titanium Oxynitride-Supported Ru Nanoparticles as Exceptional Electrocatalysts for Alkaline Hydrogen Evolution Reaction. *Chemical Engineering Journal* **2025**, *517*, 164204. https://doi.org/10.1016/j.cej.2025.164204.

(31) Liu, Z.; Zhao, S.; Liu, B.; Wang, P.; Yi, T. Multidimensional Design of Carbon-Supported Ru-Based Catalysts: A Journey to Hydrogen Evolution Reaction Performance Breakthroughs. *Chem. Sci.* **2026**, *17* (1), 52–95. https://doi.org/10.1039/D5SC06468F.

(32) El-Refaei, S. M.; Russo, P. A.; Schultz, T.; Chen, Z.; Amsalem, P.; Koch, N.; Pinna, N. Activating Ru in the Pyramidal Sites of Ru_2 P-type Structures with Earth-abundant Transition Metals for Achieving Extremely High HER Activity While Minimizing Noble Metal Content. *Carbon Energy* **2024**, *6* (9), e556. https://doi.org/10.1002/cey2.556.

(33) Xu, Y.; Du, C.; Shen, Q.; Huang, J.; Zhang, X.; Chen, J. Well-Dispersed Pyrite-Type RuS2 Nanocrystals Anchored on Porous Nitrogen and Sulfur Co-Doped Hollow Carbon Spheres for Enhanced Alkaline Hydrogen Evolution. *Chemical Engineering Journal* **2021**, *417*, 129318. https://doi.org/10.1016/j.cej.2021.129318.

(34) Su, T.; Guan, B.; Zhou, J.; Zheng, C.; Guo, J.; Chen, J.; Zhang, Y.; Yuan, Y.; Xie, W.; Zhou, N.; Dang, H.; Xu, B.; Huang, Z. Review on Ru-Based and Ni-Based Catalysts for Ammonia Decomposition: Research Status, Reaction Mechanism, and Perspectives. *Energy Fuels* **2023**, *37* (12), 8099–8127. https://doi.org/10.1021/acs.energyfuels.3c00804.

(35) Zhu, H.; Zhang, J.; Yanzhang, R.; Du, M.; Wang, Q.; Gao, G.; Wu, J.; Wu, G.; Zhang, M.; Liu, B.; Yao, J.; Zhang, X. When Cubic Cobalt Sulfide Meets Layered Molybdenum Disulfide: A Core–Shell System Toward Synergetic Electrocatalytic Water Splitting. *Advanced Materials* **2015**, *27* (32), 4752–4759. https://doi.org/10.1002/adma.201501969.

(36) Zhao, H.; Wu, J.; Chen, T.; Yan, P.; Yao, W.; Ma, X.; Sun, Y.; Wang, W.; Shi, M. Cobalt-Doped Molybdenum Sulfide as an Interlayer Facilitates Polysulfide Conversion to Obtain High-Performance Lithium−sulfur Batteries. *Journal of Energy Storage* **2024**, *101*, 113903. https://doi.org/10.1016/j.est.2024.113903.

(37) Bolagam, R.; Um, S. Hydrothermal Synthesis of Cobalt Ruthenium Sulfides as Promising Pseudocapacitor Electrode Materials. *Coatings* **2020**, *10* (3), 200. https://doi.org/10.3390/coatings10030200.

(38) Barraza Alvarez, I.; Wu, Y.; Sanchez, J.; Ge, Y.; Ramos-Garcés, M. V.; Chu, T.; Jaramillo, T. F.; Colón, J. L.; Villagrán, D. Cobalt Porphyrin

Intercalation into Zirconium Phosphate Layers for Electrochemical Water Oxidation. *Sustainable Energy Fuels* **2021**, *5* (2), 430–437. https://doi.org/10.1039/D0SE01134G.

(39) Ocuane, N.; Dorsey, B. A.; Suman, S. P.; Ramírez Ramos, M.; Banda, H.; Villagrán, D. Interface Anchoring of Cobalt Porphyrin on a Conductive Metal Organic Framework Platform for Water Electrolysis. *ACS Appl. Mater. Interfaces* **2025**, acsami.5c19333. https://doi.org/10.1021/acsami.5c19333.

(40) Li, X.; Lei, H.; Xie, L.; Wang, N.; Zhang, W.; Cao, R. Metalloporphyrins as Catalytic Models for Studying Hydrogen and Oxygen Evolution and Oxygen Reduction Reactions. *Acc. Chem. Res.* **2022**, *55* (6), 878–892. https://doi.org/10.1021/acs.accounts.1c00753.

(41) Liang, Z.; Wang, H.-Y.; Zheng, H.; Zhang, W.; Cao, R. Porphyrin-Based Frameworks for Oxygen Electrocatalysis and Catalytic Reduction of Carbon Dioxide. *Chem. Soc. Rev.* **2021**, *50* (4), 2540–2581. https://doi.org/10.1039/D0CS01482F.

(42) Ge, Y.; Lyu, Z.; Marcos-Hernández, M.; Villagrán, D. Free-Base Porphyrin Polymer for Bifunctional Electrochemical Water Splitting. *Chem. Sci.* **2022**, *13* (29), 8597–8604. https://doi.org/10.1039/D2SC01250B.

(43) Ocuane, N.; Jafari, N.; Calvillo Solis, J. J.; Saucedo, M.; Villagrán, D. Porphyrin-Functionalized Glassy Carbon Electrodes for Electrochemical Water Splitting. *Dalton Trans.* **2025**, 10.1039.D5DT01390A. https://doi.org/10.1039/D5DT01390A.

(44) Ocuane, N.; Ge, Y.; Sandoval-Pauker, C.; Villagrán, D. Bifunctional Porphyrin-Based Metal–Organic Polymers for Electrochemical Water Splitting. *Dalton Trans.* **2024**, *53* (5), 2306–2317. https://doi.org/10.1039/D3DT03371F.

(45) Joseph, M.; Haridas, S. Recent Progresses in Porphyrin Assisted Hydrogen Evolution. *International Journal of Hydrogen Energy* **2020**, *45* (21), 11954–11975. https://doi.org/10.1016/j.ijhydene.2020.02.103.

(46) Liang, Z.; Zhou, G.; Tan, H.; Mou, Y.; Zhang, J.; Guo, H.; Yang, S.; Lei, H.; Zheng, H.; Zhang, W.; Lin, H.; Cao, R. Constructing $Co_4(SO_4)_4$ Clusters within Metal–Organic Frameworks for Efficient Oxygen Electrocatalysis. *Advanced Materials* **2024**, *36* (38), 2408094. https://doi.org/10.1002/adma.202408094.

(47) Peng, X.; Han, J.; Li, X.; Liu, G.; Xu, Y.; Peng, Y.; Nie, S.; Li, W.; Li, X.; Chen, Z.; Peng, H.; Cao, R.; Fang, Y. Electrocatalytic Hydrogen Evolution with a Copper Porphyrin Bearing *Meso* -(*o* -Carborane) Substituents. *Chem. Commun.* **2023**, *59* (72), 10777–10780. https://doi.org/10.1039/D3CC03104G.

(48) Peng, X.; Zhang, M.; Qin, H.; Han, J.; Xu, Y.; Li, W.; Zhang, X.; Zhang, W.; Apfel, U.; Cao, R. Switching Electrocatalytic Hydrogen Evolution Pathways through Electronic Tuning of Copper Porphyrins. *Angewandte Chemie* **2024**, *136* (13), e202401074. https://doi.org/10.1002/ange.202401074.

(49) Li, D.; Lin, C.; Batchelor-McAuley, C.; Chen, L.; Compton, R. G. Tafel Analysis in Practice. *Journal of Electroanalytical Chemistry* **2018**, *826*, 117–124. https://doi.org/10.1016/j.jelechem.2018.08.018.

(50) Wei, C.; Sun, S.; Mandler, D.; Wang, X.; Qiao, S. Z.; Xu, Z. J. Approaches for Measuring the Surface Areas of Metal Oxide Electrocatalysts for Determining Their Intrinsic Electrocatalytic Activity. *Chem. Soc. Rev.* **2019**, *48* (9), 2518–2534. https://doi.org/10.1039/C8CS00848E.

(51) AJ Bard; LR Faulkner; HS White. *Electrochemical Methods: Fundamentals and Applications*; John Wiley & Sons, 2022.

(52) Edwards, P. H.; Bairan Espano, J. R.; Macdonald, J. E. Rational Phase Control in the Synthesis of Cobalt Sulfides. *Chem. Mater.* **2024**, *36* (15), 7186–7196. https://doi.org/10.1021/acs.chemmater.4c00911.

(53) Hu, Q. R.; Wang, S. L.; Zhang, Y.; Tang, W. H. Synthesis of Cobalt Sulfide Nanostructures by a Facile Solvothermal Growth Process. *Journal of Alloys and Compounds* **2010**, *491* (1–2), 707–711. https://doi.org/10.1016/j.jallcom.2009.11.050.

(54) Aliaga, J. A.; Araya, J. F.; Lozano, H.; Benavente, E.; Alonso-Nuñez, G.; González, G. An Easy One-Pot Solvothermal Synthesis of Poorly Crystalline Solid ReS2/C Microspheres. *Materials Chemistry and Physics* **2015**, *151*, 372–377. https://doi.org/10.1016/j.matchemphys.2014.12.012.

(55) Balakrishnan, A.; Groeneveld, J. D.; Pokhrel, S.; Mädler, L. Metal Sulfide Nanoparticles: Precursor Chemistry. *Chemistry A European J* **2021**, *27* (21), 6390–6406. https://doi.org/10.1002/chem.202004952.

(56) Zhuang, R.; Yang, J.; Wu, J. Co9S8@CNFs Cathode Enables Stable Aluminum Storage with 3D Synergy and Co-Dominated Mechanism. *Electrochemistry*

Communications **2025**, *177*, 107989. https://doi.org/10.1016/j.elecom.2025.107989.

(57) Krishnamoorthy, K.; Pazhamalai, P.; Kim, S. J. Ruthenium Sulfide Nanoparticles as a New Pseudocapacitive Material for Supercapacitor. *Electrochimica Acta* **2017**, *227*, 85–94. https://doi.org/10.1016/j.electacta.2016.12.171.

(58) Morgan, D. J. Resolving Ruthenium: XPS Studies of Common Ruthenium Materials. *Surface & Interface Analysis* **2015**, *47* (11), 1072–1079. https://doi.org/10.1002/sia.5852.

(59) Liu, H.; You, Z.; Yang, S.; Liu, C.; Xie, X.; Xiang, K.; Wang, X.; Yan, X. High-Efficient Adsorption and Removal of Elemental Mercury from Smelting Flue Gas by Cobalt Sulfide. *Environ Sci Pollut Res* **2019**, *26* (7), 6735–6744. https://doi.org/10.1007/s11356-019-04159-5.

(60) Gao, M.-R.; Liang, J.-X.; Zheng, Y.-R.; Xu, Y.-F.; Jiang, J.; Gao, Q.; Li, J.; Yu, S.-H. An Efficient Molybdenum Disulfide/Cobalt Diselenide Hybrid Catalyst for Electrochemical Hydrogen Generation. *Nat Commun* **2015**, *6* (1), 5982. https://doi.org/10.1038/ncomms6982.

(61) Sadangi, M.; Behera, J. N. Ruthenium-Doped Cobalt Sulphide Electrocatalyst Derived from a Ruthenium–Cobalt Prussian Blue Analogue (RuCo-PBA) for an Enhanced Hydrogen Evolution Reaction (HER). *Dalton Trans.* **2024**, *53* (15), 6667–6675. https://doi.org/10.1039/D4DT00099D.

(62) Cardoso, D. S. P.; Eugénio, S.; Silva, T. M.; Santos, D. M. F.; Sequeira, C. A. C.; Montemor, M. F. Hydrogen Evolution on Nanostructured Ni–Cu Foams. *RSC Adv.* **2015**, *5* (54), 43456–43461. https://doi.org/10.1039/C5RA06517H.

(63) Shinagawa, T.; Garcia-Esparza, A. T.; Takanabe, K. Insight on Tafel Slopes from a Microkinetic Analysis of Aqueous Electrocatalysis for Energy Conversion. *Sci Rep* **2015**, *5* (1), 13801. https://doi.org/10.1038/srep13801.

(64) Adiraju, A.; Jalasutram, A.; Al-Hamry, A.; Talbi, M.; Wang, J.; Tegenkamp, C.; Kanoun, O. Laser-Induced Fibers and Copper Phthalocyanine Modified Laser-Induced Graphene Electrodes for Sensitive and Selective Electrochemical Detection of Nitrite. *RSC Adv.* **2024**, *14* (39), 28648–28658. https://doi.org/10.1039/D4RA03341H.

(65) Vogt, S.; Su, Q.; Gutiérrez-Sánchez, C.; Nöll, G. Critical View on Electrochemical Impedance Spectroscopy Using the Ferri/Ferrocyanide Redox Couple at Gold Electrodes. *Anal. Chem.* **2016**, *88* (8), 4383–4390. https://doi.org/10.1021/acs.analchem.5b04814.

(66) Laschuk, N. O.; Easton, E. B.; Zenkina, O. V. Reducing the Resistance for the Use of Electrochemical Impedance Spectroscopy Analysis in Materials Chemistry. *RSC Adv.* **2021**, *11* (45), 27925–27936. https://doi.org/10.1039/D1RA03785D.

(67) Shah, K.; Dai, R.; Mateen, M.; Hassan, Z.; Zhuang, Z.; Liu, C.; Israr, M.; Cheong, W.; Hu, B.; Tu, R.; Zhang, C.; Chen, X.; Peng, Q.; Chen, C.; Li, Y. Cobalt Single Atom Incorporated in Ruthenium Oxide Sphere: A Robust Bifunctional Electrocatalyst for HER and OER. *Angew Chem Int Ed* **2022**, *61* (4), e202114951. https://doi.org/10.1002/anie.202114951.

(68) Karmakar, A.; Kundu, S. A Concise Perspective on the Effect of Interpreting the Double Layer Capacitance Data over the Intrinsic Evaluation Parameters in Oxygen Evolution Reaction. *Materials Today Energy* **2023**, *33*, 101259. https://doi.org/10.1016/j.mtener.2023.101259.

(69) Ling, C.; Li, H.-B.; Yuan, C.-Z.; Yang, Z.; Chong, H.-B.; Qian, X.-J.; Lu, X.-J.; Cheang, T.-Y.; Xu, A.-W. Sulfur Doped Ruthenium Nanoparticles as a Highly Efficient Electrocatalyst for the Hydrogen Evolution Reaction in Alkaline Media. *Catal. Sci. Technol.* **2021**, *11* (11), 3865–3872. https://doi.org/10.1039/D1CY00621E.

View Article Online
DOI: 10.1039/D6QI00499G

The data supporting this article have been included as part of the Supplementary Information.